Volume 9 | Number 3 | 7 February 2025

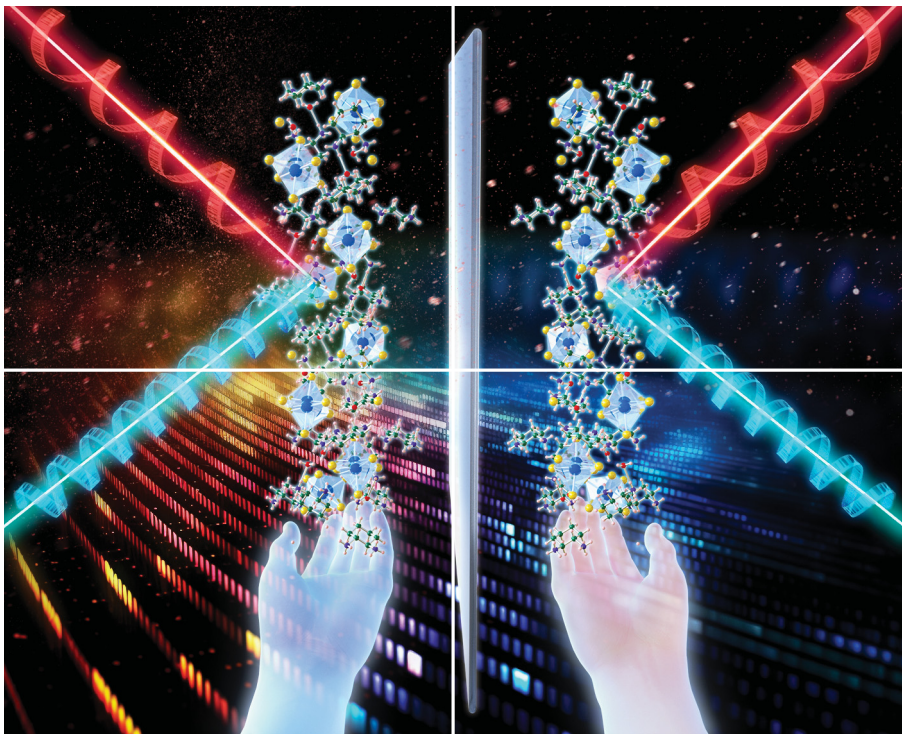

MATERIALS CHEMISTRY

FRONTIERS

CCS 中国化学会 CHINESE CHEMICAL SOCIETY
ICCAS 1956
ROYAL SOCIETY OF CHEMISTRY
rsc.li/frontiers-materials

MATERIALS CHEMISTRY FRONTIERS

CHINESE CHEMICAL SOCIETY

ROYAL SOCIETY OF CHEMISTRY

RESEARCH ARTICLE

View Article Online
View Journal | View Issue

Cite this: *Mater. Chem. Front.*, 2025, **9**, 418

Chiral 0D hybrid lead-bromide perovskites with strong nonlinear chiroptical properties†

Huan Yang,[a] Bing Sun,*[a] Junjie Guan,[b] Shun-Da Wu,[a] Peihan Wang,[b] Qiang Wang,[a] Jialiang Xu*[b] and Hao-Li Zhang*[a]

Received 15th August 2024,
Accepted 14th November 2024

DOI: 10.1039/d4qm00627e

rsc.li/frontiers-materials

Chiral optical materials enable simultaneous linear and nonlinear optical properties and have emerged as a new class of materials desirable for applications in chiroptical information technology. Herein, we developed two pairs of hybrid lead-bromide perovskites (*R*-/*S*-APD)$PbBr_4$ and (1*R*,2*R*-/1*S*,2*S*-DACH)$2PbBr_6{\cdot}2H_2O$, and systematically investigated their linear and nonlinear chiroptical responses. Second-harmonic generation circular dichroism (SHG-CD) measurements reveal a high anisotropy factor ($g_{SHG\text{-}CD}$) of up to 1.58 for (1*S*,2*S*-DACH)$_2PbBr_6{\cdot}2H_2O$, which is the highest value among those of the reported chiral perovskites to date. Notably, these perovskites display a high laser damage threshold (LDT) of up to 59.36 GW cm^{-2}. This study demonstrates that the 0D chiral hybrid lead-bromide perovskite system can simultaneously exhibit both high LDT and $g_{SHG\text{-}CD}$, thereby opening a new route for the design of high-performance chiral nonlinear optics.

Introduction

Nonlinear optical (NLO) materials are extensively used in various optical devices and play an indispensable role in laser and information technologies.[1–5] Second harmonic generation (SHG) is a nonlinear process of converting two low-frequency photons into one coherent high-frequency photon within a nonlinear medium. Such frequency-doubling processes are the key basis of many advanced applications, including all-optical switching,[6] biological microscopic imaging,[7] optical modulation[8] and quantum technology.[9] Noncentrosymmetry in crystal structures is the fundamental prerequisite for designing SHG-active materials. An effective strategy to obtain a noncentrosymmetric crystal structure is through the introduction of chiral or asymmetric organic components.[10,11]

Chiral materials are intrinsically noncentrosymmetric, and can interact differently with left- and right-handed circularly polarized light, leading to chiroptical effects such as circular dichroism (CD),[12] circularly polarized luminescence (CPL)[13,14] and SHG circular dichroism (SHG-CD).[15] Recently, great interest has been paid to chiral perovskites, which simultaneously possess inherent noncentrosymmetric structures and intrinsic chirality, and have shown attractive applications in NLO,[16–18] chiroptoelectronics[19–21] and spintronics.[22–25] Several chiral hybrid organic–inorganic perovskites based on different organic components and metals have been developed for SHG effects, including (L-ipp)PbI_3,[26] A_2BBiX_6,[27] $MHyPbBr_3$[28] (*R*/*S*-MBA)$_4Bi_2Br_{10}$,[29] (*R*/*S*-3AP)$_4AgBiBr_{12}$,[30] $MAGeBr_3$,[10] (*R*/*S*-MBA)-$CuBr_2$[15] and (*R*/*S*-MBA)BiI_4.[1] However, chiral hybrid perovskites with SHG-CD properties were not reported until very recently. The first SHG-CD of hybrid perovskites was reported on (*R*-MPEA)$_{1.5}PbBr_{3.5}(DMSO)_{0.5}$ nanowires, exhibiting an effective second-order NLO coefficient of 0.68 pm V^{-1}.[31] Subsequently, SHG-CD of the bulk single crystals of [(*R*/*S*)-3-aminopiperidine]PbI_4 showed an anisotropy factor ($g_{SHG\text{-}CD}$) of 0.21.[32] Higher $g_{SHG\text{-}CD}$ values of 0.41, 0.58 and 0.8 were achieved in copper- and bismuth-perovskite systems.[29,33,34] The first chiral hybrid germanium iodide exhibited a $g_{SHG\text{-}CD}$ of 0.48.[35] We proposed a new strategy to construct a chiral mixed halide hybrid perovskite, which showed a high $g_{SHG\text{-}CD}$ of 1.56.[36] Recently, the (*R*-MBACl)$_2PbI_4$ film was reported to exhibit a high $g_{SHG\text{-}CD}$ value of up to 1.57.[37]

Over the past years, diverse metal cations, such as Pb^{2+}, Ge^{2+}, In^{2+}, Bi^{3+} and Cu^{2+}, have been introduced to construct chiral hybrid perovskites for SHG-CD investigation.[29,31–36] Compared to other ions, Pb^{2+} ions have partially filled *d*-electron orbitals, which contribute to strong electronic polarizability and electronic transitions. Therefore, lead-containing hybrid perovskites feature strong second-order susceptibility,

[a] State Key Laboratory of Applied Organic Chemistry (SKLAOC), Key Laboratory of Special Function Materials and Structure Design (MOE), College of Chemistry and Chemical Engineering, Lanzhou University, Lanzhou 730000, P. R. China. E-mail: bingsun@lzu.edu.cn, haoli.zhang@lzu.edu.cn

[b] School of Materials Science and Engineering, Smart Sensing Interdisciplinary Science Center, Frontiers Science Center for New Organic Matter, Nankai University, 300350 Tianjin, P. R. China. E-mail: jialiang.xu@nankai.edu.cn

† Electronic supplementary information (ESI) available. CCDC 2339434, 2339435, 2339436 and 2339439. For ESI and crystallographic data in CIF or other electronic format see DOI: https://doi.org/10.1039/d4qm00627e

showing great potential in SHG-CD materials.[28,38–48] However, only two investigations on SHG-CD of lead-bromide hybrid perovskite systems have been performed, and hence the structure–property correlation is not fully understood.[31,34] Besides, lower dimensional perovskites, especially zero-dimensional (0D) hybrid perovskites, generally exhibit more pronounced nonlinear optical responses compared to their three-dimensional (3D) counterparts due to confined electron motion and strong electron–hole interaction.[49] However, the SHG-CD studies on lead-bromide perovskite systems have only been conducted on two-dimensional (2D) crystals, while that of 0D lead-bromide hybrid perovskites remains unexplored.

Herein, we report the synthesis of a 0D chiral lead-bromide hybrid perovskite, (1*R*,2*R*-/1*S*,2*S*-DACH)$_2$PbBr$_6$·2H$_2$O, as a high-performance SHG-CD material. (1*R*,2*R*-/1*S*,2*S*-DACH)$_2$PbBr$_6$·2H$_2$O was synthesized by introducing chiral cations, 1*R*,2*R*-/1*S*,2*S*-diaminocyclohexane. Meanwhile, 1D (*R*-/*S*-APD)PbBr$_4$ (*R*-/*S*-APD = *R*-/*S*-3-aminopiperidine) was also synthesized to investigate the influence of organic cations. The circular dichroism (CD) spectra of these perovskites confirmed the successful transfer of chirality from the chiral cations to the inorganic framework. (*S*-APD)PbBr$_4$ exhibited a strong SHG response across a wide excitation wavelength range from 820 nm to 1040 nm. The effective second-order nonlinear optical coefficient (d_{eff}) is up to 0.4 pm V^{-1} for (*S*-APD)PbBr$_4$. Notably, these perovskites display a high LDT of up to 59.36 GW cm^{-2}. Furthermore, a high $g_{SHG\text{-}CD}$ of 1.58 was achieved in (1*S*,2*S*-DACH)$_2$PbBr$_6$·2H$_2$O, which is the largest value among those of the reported chiral perovskites. This study demonstrates that a 0D chiral hybrid lead-bromide perovskite system can simultaneously exhibit both high $g_{SHG\text{-}CD}$ and LDT, thereby expanding the scope of chiral SHG-active materials in the field of chiral NLO.

Results and discussion

Synthesis

Fig. 1a illustrates the molecular structures of two pairs of chiral organic amines (*R*-/*S*-APD and 1*R*,2*R*-/1*S*,2*S*-DACH) utilized to synthesize chiral hybrid perovskites. Single crystals of (*R*-/*S*-APD)PbBr$_4$ and (1*R*,2*R*-/1*S*,2*S*-DACH)$_2$PbBr$_6$·2H$_2$O were synthesized according to the cooling crystallization method. Briefly, Pb(OAc)$_2$·3H$_2$O or PbO and the corresponding ammonium salt were dissolved into HBr and heated to 120 °C while stirring to afford a faint yellow solution. Slow cooling of the solutions to room temperature resulted in the formation of plate-like crystals and needle-like crystals, respectively. For the large-size crystal preparation, by employing the bottom-seeded solution growth method under an ambient atmosphere, bulk chiral single crystals of several millimeters in size were obtained,[43] as shown in Fig. 1b. The detailed synthetic process for crystal growth is described in the experimental section.

The powder X-ray diffraction (PXRD) patterns of (*R*-/*S*-APD)PbBr$_4$ and (1*R*,2*R*-/1*S*,2*S*-DACH)$_2$PbBr$_6$·2H$_2$O match well with the corresponding simulated results from the crystal structure, confirming the high phase purity of these single crystals (Fig. S1, ESI†). The PXRD spectra of these materials between those as-prepared and exposed to air for 60 days show no substantial changes, indicating their excellent ambient stability (Fig. S2, ESI†). The thermogravimetric analysis (TGA) curves of four chiral perovskites revealed decomposition temperatures higher than 580 K (Fig. S3, ESI†), suggesting their high thermostability is comparable to that of the chiral lead halide perovskites.[31,50,51] In Fig. S3c and d (ESI†), the first weight loss observed in (1*R*,2*R*-/1*S*,2*S*-DACH)$_2$PbBr$_6$·2H$_2$O can be attributed to the loss of coordinated H$_2$O in the crystals, while the second weight loss corresponds to their decomposition.

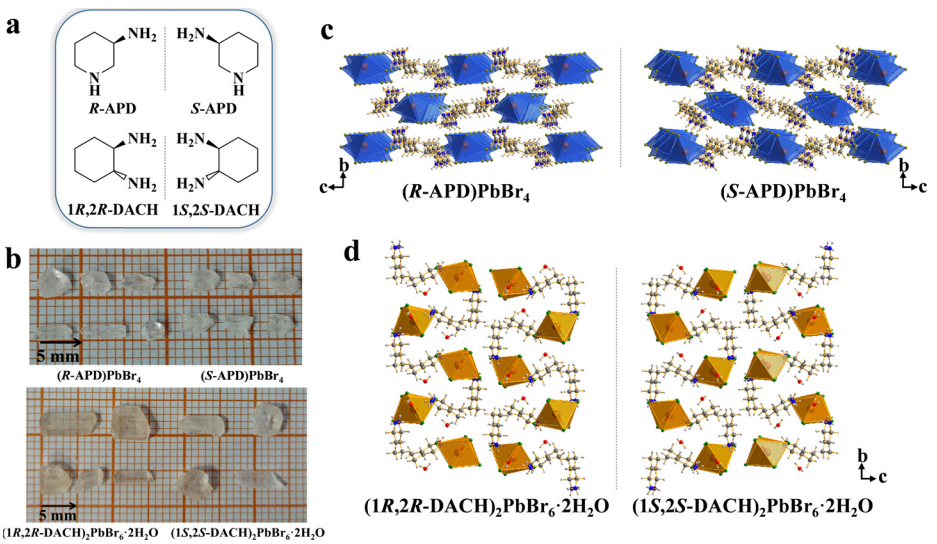

Fig. 1 (a) Molecular structures of the *R*-APD, *S*-APD, 1*R*,2*R*-DACH and 1*S*,2*S*-DACH (*R*-/*S*-APD = *R*/*S*-3-aminopiperidine, 1*R*,2*R*-/1*S*,2*S*-DACH = 1*R*,2*R*-/1*S*,2*S*-diaminocyclohexane). (b) The photographs of (*R*-/*S*-APD)PbBr$_4$ and (1*R*,2*R*-/1*S*,2*S*-DACH)$_2$PbBr$_6$·2H$_2$O single crystals (the scale bar is 5 mm). (c) Crystal structures of (*R*-APD)PbBr$_4$ and (*S*-APD)PbBr4. (d) Crystal structures of (1*R*,2*R*-DACH)$_2$PbBr$_6$·2H$_2$O and (1*S*,2*S*-DACH)$_2$PbBr$_6$·2H$_2$O. The crystals were viewed along the *a*-axis.

The remarkable environmental stability and thermostability of these chiral hybrid perovskite crystals make them promising candidates for practical applications in nonlinear optics.

Crystal structures

The crystal structures of (*R*-/*S*-APD)$PbBr_4$ and (1*R*,2*R*-/1*S*,2*S*-DACH)$_2PbBr_6{\cdot}2H_2O$ were analyzed using single-crystal X-ray diffraction. The crystal data and structure refinement are provided in Tables S1–S4 (ESI†).

Fig. 1c illustrates the crystal structures of (*R*-APD)$PbBr_4$ and (*S*-APD)$PbBr_4$, which feature one-dimensional (1D) structures. This 1D structure that combines edge-sharing chains resulted from the use of the *R*-/*S*-APD cation in (*R*-/*S*-APD)$PbBr_4$, which is similar to that found in (2,6-dmpz)$_3Pb_2Br_{10}$.[52,53] (*R*-APD)$PbBr_4$ and (*S*-APD)$PbBr_4$ adopt the noncentrosymmetric orthorhombic space group of $P2_12_12_1$ with unit cell parameters a = 8.7802 Å, b = 10.8321 Å, c = 13.9609 Å and a = 8.7810 Å, b = 10.8005 Å, c = 13.7783 Å, respectively. The crystal structure consists of $[PbBr_6]_\infty^{4-}$ chains sitting in the columnar cages composed of $(R\text{-}/S\text{-APD})^{2+}$ cations. The ammonium moieties hydrogen bond to bromide ions (Fig. S4, ESI†) with N···Br distances ranging from 2.613 to 2.820 Å. The inorganic chain is based on edge-shared octahedral $[PbBr_6]^{4-}$ moieties (Fig. S5a and b, ESI†), which are different from the typical corner-sharing octahedral units found in 2D and 3D hybrid perovskites.[27,54] The inorganic chain is then separated and charge-balanced by $(R\text{-}/S\text{-APD})^{2+}$ cations, as shown in Fig. S5c and d (ESI†). Then, inorganic chains and organic components are arranged alternately to form the 1D crystal structure. This structure can be considered as the bulk assembly of 1D core–shell quantum wires, in which the insulating organic shells surround the core copper chloride wires.[55]

An exotic type of 0D structure that contains isolated $[PbBr_6]^{4-}$ octahedron resulted from the use of the 1*R*,2*R*-/1*S*,2*S*-DACH cation in (1*R*,2*R*-/1*S*,2*S*-DACH)$_2PbBr_6{\cdot}2H_2O$. Fig. 1d shows the crystal structures of (1*R*,2*R*-DACH)$_2PbBr_6{\cdot}2H_2O$ and (1*S*,2*S*-DACH)$_2PbBr_6{\cdot}2H_2O$, which exhibit a mirror image relationship with each other. The orthorhombic space group $P2_12_12_1$ governs the (1*R*,2*R*-DACH)$_2PbBr_6{\cdot}2H_2O$ and (1*S*,2*S*-DACH)$_2PbBr_6{\cdot}2H_2O$ crystallization, with unit cell parameters of a = 9.8774 Å, b = 10.8539 Å, c = 24.3071 Å and a = 9.9329 Å, b = 10.9337 Å, c = 24.3960 Å, respectively. The adjacent $[PbBr_6]^{4-}$ octahedrons are spatially separated by organic amines and H_2O molecules, resulting in a typical 0D organic–inorganic hybrid structure. Each asymmetry unit of (1*R*,2*R*-DACH)$_2PbBr_6{\cdot}2H_2O$ and (1*S*,2*S*-DACH)$_2PbBr_6{\cdot}2H_2O$ contains an inorganic octahedron $[PbBr_6]^{4-}$, two organic amine cations $(1R,2R\text{-}/1S,2S\text{-DACH})^{2+}$ and two H_2O molecules (Fig. S6a and b, ESI†). The 0D inorganic framework is primarily supported by N–H···Br hydrogen bonds and O–H···Br hydrogen bonds (Fig. S7, ESI†) between the organic cations, inorganic octahedrons and H_2O molecules. These hydrogen bonds formed by the introduction of chiral amine cations $(1R,2R\text{-}/1S,2S\text{-DACH})^{2+}$ could affect the distortion level of inorganic $[PbBr_6]^{4-}$ octahedron (as discussed below).[56]

Structural distortion is commonly present in the perovskite structure, as for these two pairs of compounds, which is evaluated by the level of distortion of the $[PbBr_6]^{4-}$ octahedron. The distortion level (Δd) of inorganic $[PbBr_6]^{4-}$ octahedron can be quantitatively calculated based on the length of Pb–Br using the following eqn (1),[57,58]

$$\Delta d = \frac{1}{6}\sum_{i=1}^{6}\left[\frac{d_i - d}{d}\right]^2 \quad (1)$$

where d is the average bond length of the Pb–Br bond and d_i is the bond length of the six individual Pb–Br bonds. The Pb–Br bond length is marked in Fig. S8 (ESI†) and the Δd values are summarized in Table S5 (ESI†). The results suggest that the $[PbBr_6]^{4-}$ octahedron is significantly distorted with Pb atoms deviating from the balanced sites. For (*R*-APD)$PbBr_4$ and (*S*-APD)$PbBr_4$, the Δd is calculated to be 2.05×10^{-3} and 1.86×10^{-3}, respectively. This Δd is smaller than that of previously reported chiral 1D hybrid perovskite, which indicates smaller octahedral distortion.[59,60] The values of Δd are calculated to be 1.4×10^{-4} for (1*R*,2*R*-DACH)$_2PbBr_6{\cdot}2H_2O$ and 1.34×10^{-4} for (1*S*,2*S*-DACH)$_2PbBr_6{\cdot}2H_2O$, respectively, indicating that there is no substantial difference in structural distortion between these two enantiomers. In comparison, the (*R*-/*S*-APD)$PbBr_4$ octahedrons have higher Δd values than (1*R*,2*R*-/1*S*,2*S*-DACH)$_2PbBr_6{\cdot}2H_2O$, which illustrates the formation of greater distortion in the octahedrons.

Electronic properties

To investigate the linear optical and chiroptical properties of (*R*-/*S*-APD)$PbBr_4$ and (1*R*,2*R*-/1*S*,2*S*-DACH)$_2PbBr_6{\cdot}2H_2O$ crystals, the crystals were thoroughly ground with KBr and pressed into pellets. The UV-vis-NIR absorption and CD spectra of chiral hybrid perovskites are shown in Fig. 2, with peak positions mainly distributed in the ultraviolet region. The solid UV-vis-NIR optical absorption spectra of (*R*-APD)$PbBr_4$ and (*S*-APD)$PbBr_4$ are presented in Fig. 2a, displaying a similar profile with absorption peaks at 324 nm. The absorption of 1D Pb–Br hybrid perovskite is mainly in the UV region, previously shown in other 1D Pb–Br systems such as $C_4N_2H_{14}PbBr_4$[61] and [(H_2O)-$(C_6H_8N_3)_2Pb_2Br_{10}$].[62] For (1*R*,2*R*-DACH)$_2PbBr_6{\cdot}2H_2O$ and (1*S*,2*S*-DACH)$_2PbBr_6{\cdot}2H_2O$, the absorption peaks were observed at 315 nm, as shown in Fig. 2b. The absorption peak observed at 315 nm was attributed to the ligand-to-metal charge transfer band of $[PbBr_6]^{4-}$. The bandgaps were estimated by extrapolating the high-energy slope to the imaginary axis parallel to the x-axis, where the absorption edge is interrupted by the exciton peak.[63] The corresponding optical bandgap energies are 3.33 eV, 3.33 eV, 3.61 eV and 3.61 eV for (*R*-APD)$PbBr_4$, (*S*-APD)$PbBr_4$, (1*R*,2*R*-DACH)$_2PbBr_6{\cdot}2H_2O$ and (1*S*,2*S*-DACH)$_2PbBr_6{\cdot}2H_2O$, respectively (Fig. S9, ESI†).

CD signals of (*R*-APD)$PbBr_4$ and (*S*-APD)$PbBr_4$ appear at the same wavelengths of 287 nm and 347 nm but with opposite signs. The enantiomeric perovskites of (1*R*,2*R*-DACH)$_2PbBr_6{\cdot}2H_2O$ and (1*S*,2*S*-DACH)$_2PbBr_6{\cdot}2H_2O$ also exhibit similar positions but oppositely signed CD patterns at 267 nm and 324 nm. The CD signals of organic ammonium salts *R*-/*S*-APD·2HCl and 1*R*,2*R*-/1*S*,2*S*-DACH·2HCl appear at approximately 261 nm and 264 nm (Fig. S10, ESI†), respectively. The CD signals for these chiral organic ammonium salts are mainly located lower than 300 nm.

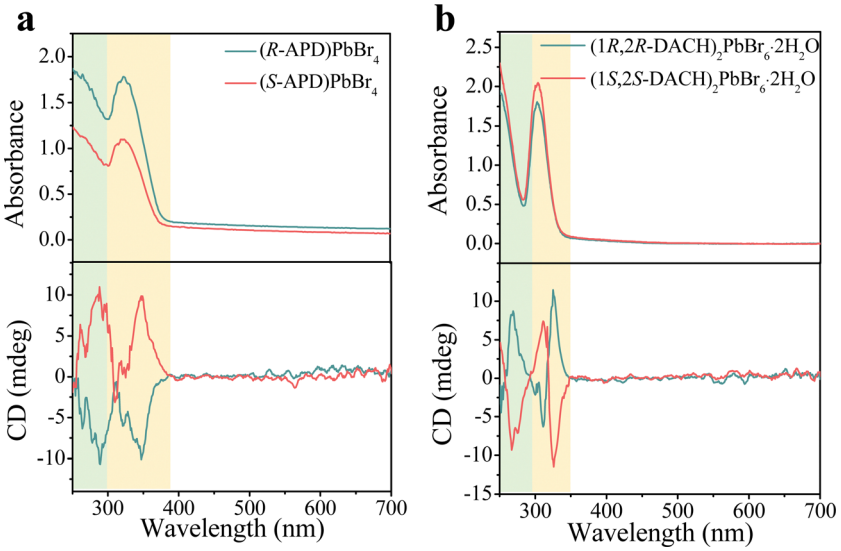

Fig. 2 UV-vis-NIR absorption spectra and circular dichroism (CD) spectra of (a) (*R*-APD)$PbBr_4$ and (*S*-APD)$PbBr_4$, and (b) (1*R*,2*R*-DACH)$_2PbBr_6{\cdot}2H_2O$ and (1*S*,2*S*-DACH)$_2PbBr_6{\cdot}2H_2O$.

However, when they are incorporated into the chiral perovskites, the resulting perovskites exhibit opposite CD values in the visible region higher than 300 nm. These observations indicate that chirality is successfully transferred from the chiral organic cations to the perovskites.[33] The CD spectra of the (*R*-APD)$PbBr_4$ and (*S*-APD)$PbBr_4$ exhibit absorption peaks mainly centered in two regions: one is from 250 nm to 300 nm, and the other is from 300 nm to 380 nm. Similarly, (1*R*,2*R*-DACH)$_2PbBr_6{\cdot}2H_2O$ and (1*S*,2*S*-DACH)$_2PbBr_6{\cdot}2H_2O$ also exhibit two CD signal regions, ranging from 250 nm to 290 nm and from 290 nm to 350 nm, respectively. In each region, bisignate CD signals can be observed from one configuration with two peaks, which is attributed to the splitting of the energy state with the opposite spin states of electrons.[64,65] Such bisignate CD signals correspond to one absorption peak in the related absorption spectra and is usually interpreted as the Cotton effect, meaning that the chiral perovskites exhibit characteristic CD signals at the highest absorption wavelengths since they have different absorption coefficients to left-handed circularly polarized (LCP) and right-handed circularly polarized (RCP) lights.[66,67] In addition, the g_{CD} spectra of these chiral perovskites can be calculated by using the following equation[68]

$$g_{CD} = \frac{\mathrm{CD(mdeg)}}{32\,980 \times \mathrm{Absorbance}} \quad (2)$$

The maximum g_{CD} are -1.27×10^{-4} and 1.34×10^{-4} at 350 nm for (*R*-APD)$PbBr_4$ and (*S*-APD)$PbBr_4$, and 6.55×10^{-4} and -6.75×10^{-4} at 362 nm for (1*R*,2*R*-DACH)$_2PbBr_6{\cdot}2H_2O$ and (1*S*,2*S*-DACH)$_2PbBr_6{\cdot}2H_2O$ (Fig. S11, ESI†), which are comparable to other lead-based perovskites.[69,70]

To further understand the electronic band structures and density of states (DOS) of the chiral hybrid perovskites, first-principles calculations based on density functional theory (DFT) were performed. The bandgaps of (*S*-APD)$PbBr_4$ and (1*S*,2*S*-DACH)$_2PbBr_6{\cdot}2H_2O$ were determined to be 3.35 eV and 3.65 eV, respectively, as shown in Fig. 3a and b. For (*R*-APD)$PbBr_4$ and (1*R*,2*R*-DACH)$_2PbBr_6{\cdot}2H_2O$, the bandgaps were 3.39 eV and 3.68 eV, as shown in Fig. S12a and S12b (ESI†), respectively. The calculated bandgap is consistent with the observed optical bandgap taken from the absorption spectra (Fig. S9, ESI†). According to the partial DOS of (*R*-/*S*-APD)$PbBr_4$ and (1*R*,2*R*-/1*S*,2*S*-DACH)$_2PbBr_6{\cdot}2H_2O$, the conduction band minimum (CBM) is derived mainly from the Br and Pb orbitals, whereas the valence band maximum (VBM) comprises Br orbitals, as shown in Fig. 3c and d. The calculated energy band structure reveals that the CBM is localized at the Γ point, while the VBM is localized at the S point, indicating an indirect band gap for (*S*-APD)$PbBr_4$. Moreover, both the CBM and VBM are located at Γ points, indicating a direct band gap of (1*S*,2*S*-DACH)$_2PbBr_6{\cdot}2H_2O$.

SHG properties

The introduction of chiral organic cations to an inorganic framework disrupts the centrosymmetric structures of the perovskites that endow the perovskites with SHG properties. The wavelength- and powder-dependent SHG measurements were conducted and the influence of different chiral organic amines on the SHG effect was also analyzed. For the SHG measurements, we utilized a homemade microscope equipped with a femtosecond pulsed laser as the pump source. Fig. 4a illustrates the schematic diagram of the SHG measurements, where $\lambda/2$ and $\lambda/4$ plates are employed to adjust the linearly polarized and circularly polarized angles, respectively. Fig. S13a (ESI†) shows the intensity of SHG mapping for (*S*-APD)$PbBr_4$, obtained at 520 nm when pumped at 1040 nm. For (1*S*,2*S*-DACH)$_2PbBr_6{\cdot}2H_2O$, the mapping detects the SHG signal at 440 nm when pumped at 880 nm (Fig. S13b, ESI†). The mapping image demonstrates the crystal morphology and SHG activity of the single crystal. Fig. 4b and c present the wavelength-dependent SHG spectra collected from the (*S*-APD)-$PbBr_4$ and (1*S*,2*S*-DACH)$_2PbBr_6{\cdot}2H_2O$ crystals, respectively,

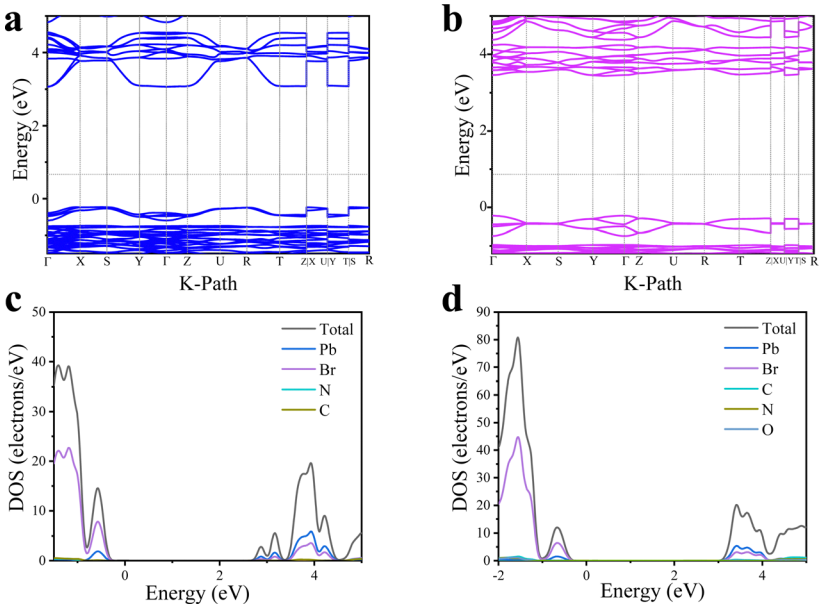

Fig. 3 (a) and (b) Calculated electronic band structures of (*S*-APD)$PbBr_4$ and (1*S*,2*S*-DACH)$_2PbBr_6{\cdot}2H_2O$. (c) and (d) Calculated partial DOS of (*S*-APD)$PbBr_4$ and (1*S*,2*S*-DACH)$_2PbBr_6{\cdot}2H_2O$.

when pumped at various wavelengths with the same excitation power at 50 mW. The (*S*-APD)$PbBr_4$ crystals exhibit SHG responses across a wide range of wavelengths and exhibit the highest SHG intensity when pumped at 940 nm. The wavelength-dependent SHG spectra of (1*S*,2*S*-DACH)$_2PbBr_6{\cdot}2H_2O$ exhibit distinct SHG signals when the excitation wavelength is tuned between 940 nm and 1040 nm in 20 nm steps. Notably, when pump light is set at 1020 nm, the (1*S*,2*S*-DACH)$_2PbBr_6{\cdot}2H_2O$ single crystal exhibits the strongest SHG signal collected at 510 nm.

Power-dependence SHG intensities of (*S*-APD)$PbBr_4$ and (1*S*,2*S*-DACH)$_2PbBr_6{\cdot}2H_2O$ are presented in Fig. 4d and e. The intensity of the SHG signals scales quadratically with the power of the pump, which is consistent with previous literature reports.[15,29,51] This observation further confirms the two-photon nature of the second-order NLO response. Remarkably, the synthesized chiral perovskites exhibit a large LDT, and the SHG intensity remains in line with the fitted linear relationship until the pump power reaches approximately 1392 mW for (*S*-APD)$PbBr_4$ and 1362 mW for (1*S*,2*S*-DACH)$_2PbBr_6{\cdot}2H_2O$. This power can be considered as the LDT of chiral perovskites, which corresponds to the excitation power of (*S*-APD)$PbBr_4$ at 59.36 GW cm^{-2} and (1*S*,2*S*-DACH)$_2PbBr_6{\cdot}2H_2O$ at 54.22 GW cm^{-2}. The pulse width, repetition rate and laser spot are ~100 fs, ~80 MHz and ~20 μm in diameter, respectively.[36,71] Notably, these LDT values are larger than those of most previously reported chiral metal perovskites (Fig. S14 and Table S6, ESI†). This observation indicates that the synthesized chiral perovskites possess high laser stability, and thus show great promise for investigating the nonlinear chiroptical devices.

The SHG intensity $I_{2\omega}$ can be calculated according to eqn (3):[72,73]

$$I_{2\omega} = \frac{2\omega^2}{c^3 n_\omega^2 n_{2\omega} \varepsilon_0} \frac{\sin(\Delta k L/2)^2}{(\Delta k L/2)^2} I_\omega^2 (d_{\text{eff}} L)^2 \quad (3)$$

where L is the microplate thickness, Δk is the wave-vector difference, d_{eff} is the second-order NLO coefficient, n_ω and $n_{2\omega}$ indicate the refractive index of waves, and I_ω and $I_{2\omega}$ are the laser irradiance at ω and 2ω, respectively. To evaluate the second-order NLO coefficient (d_{eff}) of chiral hybrid perovskites, we utilized a commercial Y-cut quartz with a d_{eff} of 0.3 pm V^{-1} as the reference. The NLO coefficient is estimated according to eqn (4)[33,35,74]

$$\frac{d_{\text{eff}(S)}}{d_{\text{eff(ref)}}} \approx \frac{L_S}{L_{\text{ref}}} \frac{P_{\text{in(ref)}}}{P_{\text{in}(S)}} \sqrt{\frac{I_{\text{out}(S)}}{I_{\text{out(ref)}}}} \quad (4)$$

where the superscripts "*S*" and "ref" refer to the *S*-samples and Y-cut quartz, L is the effective crystal thickness, P_{in} represents the incident light intensity, and I_{out} represents the output intensity of SHG. During the SHG measurement, both the *S*-samples and Y-cut quartz were characterized under the same laser conditions. Based on the test data, the SHG intensity of (*S*-APD)$PbBr_4$ and (1*S*,2*S*-DACH)$_2PbBr_6{\cdot}2H_2O$ is 1.8 times and 0.2 times that of Y-cut quartz when pumped at 1000 nm, as shown in Fig. 4f. The SHG intensities of (*S*-APD)$PbBr_4$ and (1*S*,2*S*-DACH)$_2PbBr_6{\cdot}2H_2O$ are 2 times and 0.22 times that of Y-cut quartz (Fig. S15, ESI†), respectively, when pumped at 1020 nm, which are similar with that pumped at 1000 nm. Then, we determined the absolute d_{eff} of the (*S*-APD)$PbBr_4$ and (1*S*,2*S*-DACH)$_2PbBr_6{\cdot}2H_2O$ to be 0.4 pm V^{-1} and 0.13 pm V^{-1}, respectively. Compared with (1*S*,2*S*-DACH)$_2PbBr_6{\cdot}2H_2O$, (*S*-APD)$PbBr_4$ has a larger d_{eff}. This increase in SHG intensity could also be attributed to the greater octahedral distortion in (*S*-APD)$PbBr_4$ crystals than in (1*S*,2*S*-DACH)$_2PbBr_6{\cdot}2H_2O$.[36]

Polarization-dependent SHG responses of (*S*-APD)$PbBr_4$ and (1*S*,2*S*-DACH)$_2PbBr_6{\cdot}2H_2O$ collected at 450 nm and 520 nm are shown in Fig. 5a and b. The plots exhibit a dipolar profile that

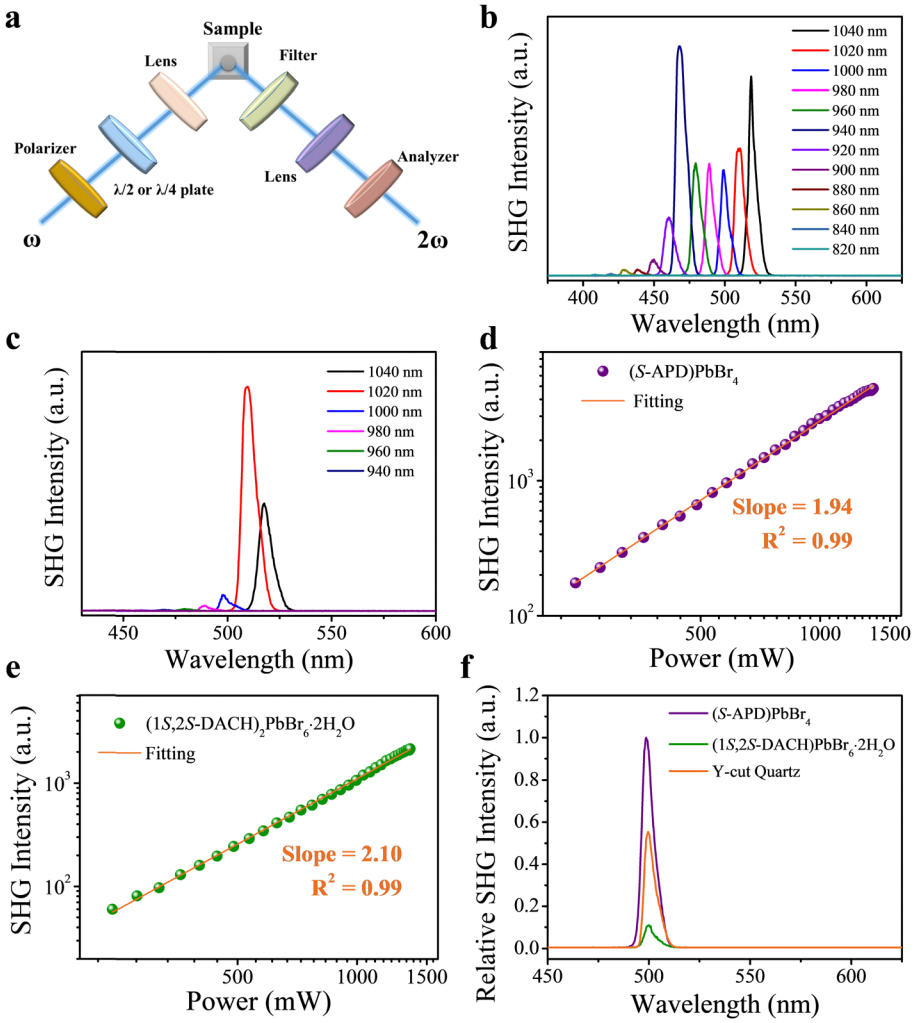

Fig. 4 (a) Schematic diagram of the SHG measurements. The $\lambda/2$ and $\lambda/4$ plates are used for tuning linearly polarized and circularly polarized angles, respectively. (b) and (c) NLO spectra of the (*S*-APD)$PbBr_4$ crystals and (1*S*,2*S*-DACH)$_2PbBr_6{\cdot}2H_2O$ crystals pumped at various wavelengths. (d) The logarithmic plot of SHG intensity as a function of the incident power of (*S*-APD)$PbBr_4$ crystals pumped at 860 nm. The solid line is a linear fitting with a slope of 1.94. (e) The logarithmic plot of SHG intensity as a function of the incident power of (1*S*,2*S*-DACH)$_2PbBr_6{\cdot}2H_2O$ crystals pumped at 900 nm. The solid line is a linear fitting with a slope of 2.10. (f) A comparison of the SHG signal intensities of (*S*-APD)$PbBr_4$ and (1*S*,2*S*-DACH)$_2PbBr_6{\cdot}2H_2O$ crystals and Y-cut quartz at 1000 nm under the same test conditions.

fits well to a $\cos^4\theta$ function. The corresponding polarization ratio ρ can be calculated by using the following eqn (5):

$$\rho = \frac{I_{max} - I_{min}}{I_{max} + I_{min}} \quad (5)$$

where I_{max} and I_{min} are the maximum and minimum values of SHG intensity.[51] The calculated polarization ratio ρ was determined to be 94.23% and 85.63% for (*S*-APD)$PbBr_4$ and (1*S*,2*S*-DACH)$_2PbBr_6{\cdot}2H_2O$, respectively. The polarization-dependent SHG response of (*S*-APD)$PbBr_4$ was also tested at 1040 nm and the corresponding polarization ratio ρ was 90.4% (Fig. S16, ESI†). This result indicates a significant difference in the SHG response between different polarization states for these chiral perovskites. Subsequently, we further studied the NLO chiroptical effects of chiral perovskites by measuring the SHG-CD, which is defined as the normalized difference between SHG intensities obtained with left-handed circularly polarized (LCP) and right-handed circularly polarized (RCP) light excitations. By replacing the $\lambda/2$ plate with a $\lambda/4$ plate (Fig. 4a), we tuned the fundamental laser pump from linearly polarized to LCP or RCP. As depicted in Fig. 5c and d, the SHG intensity was changed following the rotation of the $\lambda/4$ plate. In particular, the SHG intensity of (*S*-APD)$PbBr_4$ and (1*S*,2*S*-DACH)$_2PbBr_6{\cdot}2H_2O$ was stronger under RCP excitation compared to LCP excitation. In contrast, the SHG intensity of (*R*-APD)$PbBr_4$ and (1*R*,2*R*-DACH)$_2PbBr_6{\cdot}2H_2O$ under a left-handed circularly polarized laser was stronger than that under a right-handed circularly polarized laser (Fig. S17, ESI†). These observations demonstrate the presence of SHG-CD in the chiral perovskites, indicating a strong coupling between the chiral organic cations and the inorganic framework, leading to the emergence of chiroptical properties.

Then, to quantify the SHG-CD effect of these chiral hybrid lead-bromide perovskites, the $g_{SHG\text{-}CD}$ was calculated based on

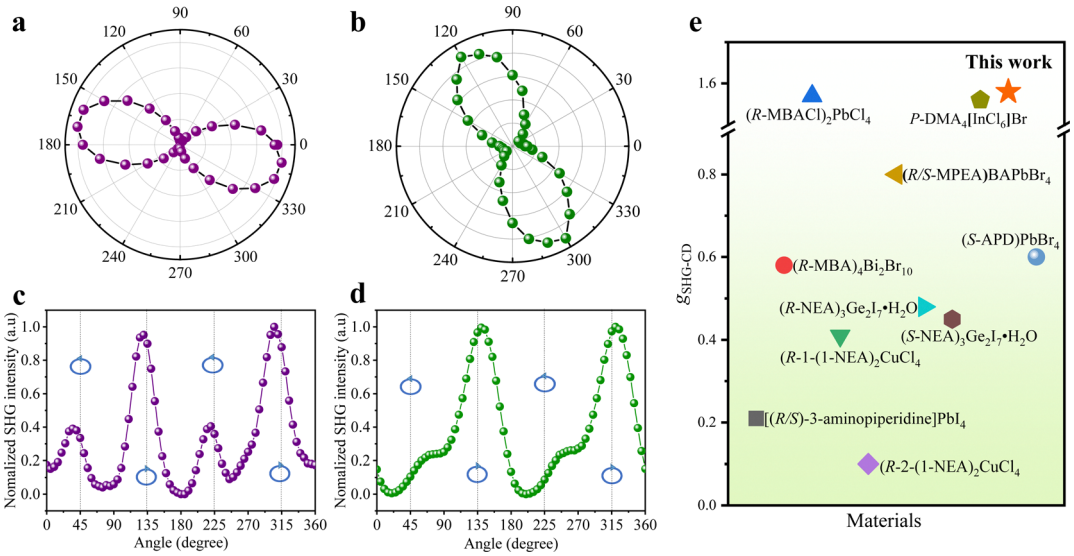

Fig. 5 (a) and (b) Polarization dependence of the SHG intensity of (*S*-APD)$PbBr_4$ and (1*S*,2*S*-DACH)$_2PbBr_6{\cdot}2H_2O$ crystals as a function of the linear polarization angle pumped at 900 nm and 1040 nm, respectively. The purple and green line is the nonlinear fitting of data points. (c) and (d) SHG intensity of (*S*-APD)$PbBr_4$ and (1*S*,2*S*-DACH)$_2PbBr_6{\cdot}2H_2O$ crystals at various elliptic polarized angles under 1040 nm laser. The laser is left-handed circularly polarized when the rotation angles are 45 and 225°, while it is right-handed circularly polarized at 135 and 315°, as indicated by the blue arrows. (e) Comparison of $g_{SHG\text{-}CD}$ in the literature and in this work.

eqn (6):[29,33,75]

$$g_{SHG\text{-}CD} = \frac{2|I_{LCP} - I_{RCP}|}{I_{LCP} + I_{RCP}} \quad (6)$$

where I_{LCP} and I_{RCP} denote the SHG intensities excited by left- and right-handed circularly polarized lasers, respectively. The $g_{SHG\text{-}CD}$ values of the chiral hybrid perovskites are summarized in Table S7 (ESI†), and the (1*S*,2*S*-DACH)$_2PbBr_6{\cdot}2H_2O$ possesses a $g_{SHG\text{-}CD}$ value of 1.58, which is higher than that of (*S*-APD)$PbBr_4$ with a $g_{SHG\text{-}CD}$ value of 0.6. Combining the CD and SHG-CD measurements, both the g_{CD} and $g_{SHG\text{-}CD}$ values indicate a consistent trend, that the (1*S*,2*S*-DACH)$_2PbBr_6{\cdot}2H_2O$ exhibit much higher chiral effects than (*S*-APD)$PbBr_4$ in either linear or nonlinear optical responses. Fig. 5e illustrates the recent progress in representative chiral perovskite materials and their $g_{SHG\text{-}CD}$ values. Notably, (1*S*,2*S*-DACH)$_2PbBr_6{\cdot}2H_2O$ exhibits the highest $g_{SHG\text{-}CD}$ among reported chiral hybrid perovskites. This high $g_{SHG\text{-}CD}$-featured chiral hybrid perovskite shows promise for application in circularly polarized light detection.

The different values of $g_{SHG\text{-}CD}$ for (*S*-APD)$PbBr_4$ and (1*S*,2*S*-DACH)$_2PbBr_6{\cdot}2H_2O$ indicate that the SHG-CD properties of chiral organic–inorganic hybrid perovskite materials are modulated by the organic cations. In the study of nonlinear optics in a hybrid perovskite system, the dimensionality of the crystal is one important factor in determining the intensity of SHG-CD responses.[59] For chiral hybrid perovskites, the large cation radii of chiral organic molecules render them devoid of connectivity between the metal-halide octahedra, thus lowering their structural dimensionality.[1] Having two or more chiral centers in one chiral molecule could have a strong impact on many chiral properties, including tunable signal reversal of circular dichroism,[76] enhanced interactions with polarized light[77] and dynamic light multiplexing.[78] In this work, by utilizing large volume double chiral center amines 1*R*,2*R*-/1*S*,2*S*-DACH, 0D structures of chiral perovskites (1*R*,2*R*-/1*S*,2*S*-DACH)$_2PbBr_6{\cdot}2H_2O$ were obtained.[79,80] 1D structures of (*R*-/*S*-APD)$PbBr_4$ were synthesized by employing *R*-/*S*-APD. Using double chiral center amines, low-dimensional hybrid perovskites can be obtained. These lower-dimensional perovskites often exhibit stronger SHG-CD effects because of the larger spatial separation between organic and inorganic components, leading to a pronounced dipole moment. Also, such a low-dimensional structure in (1*S*,2*S*-DACH)$_2PbBr_6{\cdot}2H_2O$ gives rise to strong electron–phonon coupling, which enables the possible realization of the enhancement of the SHG-CD effect.[1] To evaluate the electron–phonon coupling of (*S*-APD)$PbBr_4$ and (1*S*,2*S*-DACH)$_2PbBr_6{\cdot}2H_2O$, we calculated the temperature dependence of the band gap renormalization (Fig. S19–S23, ESI†).[81] (*S*-APD)$PbBr_4$ and (1*S*,2*S*-DACH)$_2PbBr_6{\cdot}2H_2O$ exhibit phonon-induced zero-point renormalizations reaching 77 meV and 144 meV, respectively. These results indicate (*S*-APD)$PbBr_4$ and (1*S*,2*S*-DACH)$_2PbBr_6{\cdot}2H_2O$ have strong electron–phonon coupling.[82] Additionally, the band gap renormalization is significantly influenced by temperature (Fig. S19–S23, ESI†). Notably, (1*S*,2*S*-DACH)$_2PbBr_6{\cdot}2H_2O$ demonstrates stronger electron–phonon coupling, as evidenced by the higher zero-point renormalization and more pronounced temperature dependence of the band gap renormalization.

Furthermore, from the crystal cell structure of (1*S*,2*S*-DACH)$_2PbBr_6{\cdot}2H_2O$, there are 8 chiral cations. However, only 4 chiral cations are contained in (*S*-APD)$PbBr_4$ (Fig. S24, ESI†). As the noncentrosymmetric crystal structure is obtained by the introduction of chiral cations, more chiral amines lead to stronger asymmetry in (1*S*,2*S*-DACH)$_2PbBr_6{\cdot}2H_2O$ than

(*S*-APD)$PbBr_4$. Therefore, such a high value of $g_{SHG\text{-}CD}$ in (1*S*,2*S*-DACH)$_2PbBr_6{\cdot}2H_2O$ primarily originates from the lower dimensional (0D) structure of the Pb-based chiral perovskites, where the chiral ligands per volume will be significantly more than in the 1D counterparts.[83] Overall, low-dimensional structures and stronger asymmetry lead to improved SHG-CD performance and thus a higher $g_{SHG\text{-}CD}$ value. This property–structure relationship analysis provides new insights for designing low dimensional and fine-tuning of the SHG-CD properties in chiral hybrid perovskite materials.

Recent investigations have shown that the g_{CD} of organic–inorganic hybrid perovskites is highly sensitive to the material's dimensionality.[84,85] In 1D hybrid perovskites, the structure is confined along one dimension. The increased confinement and reduced dimensionality promote stronger interactions between the chiral organic cations and excitons, leading to a significant enhancement in the circular dichroism response.[86–88] However, in 0D perovskites, the excitons are completely confined, leading to discrete energy levels. As a consequence, the anisotropy factor in the CD spectra is generally enhanced as the dimensionality is reduced from 1D to 0D.[89] For the SHG-CD effect, compared to 1D hybrid perovskites, 0D crystals have stronger confinement effects that can enhance the electric dipole interactions, and increase the anisotropy. Additionally, stronger quantum confinement in 0D structures can also lead to an enhanced SHG-CD effect, because of altered electronic band structures and increased light–matter interaction at the interface.[90]

Conclusions

In summary, we have successfully designed and synthesized two pairs of chiral hybrid perovskites, (*R*-/*S*-APD)$PbBr_4$ and (1*R*,2*R*-/1*S*,2*S*-DACH)$_2PbBr_6{\cdot}2H_2O$. Furthermore, (1*S*,2*S*-DACH)$_2PbBr_6{\cdot}2H_2O$ exhibits a remarkable $g_{SHG\text{-}CD}$ of 1.58, which is the highest value among the reported chiral hybrid perovskites. This high $g_{SHG\text{-}CD}$ can be attributed to the material's unique 0D crystal structure, which enhances the asymmetry of (1*S*,2*S*-DACH)$_2PbBr_6{\cdot}2H_2O$. Additionally, these chiral hybrid lead bromide perovskites exhibited strong nonlinear chiroptical effects, with the effective second-order NLO coefficient reaching up to 0.4 pm V^{-1} for (*S*-APD)$PbBr_4$ and 0.13 pm V^{-1} for (1*S*,2*S*-DACH)$_2PbBr_6{\cdot}2H_2O$. The LDT is as high as 59.36 GW cm^{-2} for (*S*-APD)$PbBr_4$, which is one of the largest values among the chiral hybrid perovskites. Our work demonstrates that the 0D chiral hybrid lead-bromide perovskite system can achieve both high $g_{SHG\text{-}CD}$ and LDT, expanding the range of chiral SHG-active materials towards chiral nonlinear optical application.

Author contributions

H. L. Zhang and B. Sun conceived the idea for the manuscript and designed the experiments. H. Yang synthesized the materials and conducted the SCXRD, UV-vis-NIR absorption spectra and circular dichroism spectra. S. D. Wu contributed to the theoretical calculations. H. Yang, J. Guan and P. Wang contributed to the SHG measurements. H. L. Zhang, J. Xu, B. Sun and Q. Wang discussed the results and commented on the manuscript at all stages. H. L. Zhang led the project.

Data availability

All experimental and characterization data are available in the ESI.†

Conflicts of interest

The authors declare no conflicts of interest.

Acknowledgements

This work was supported by the National Natural Science Foundation of China (NSFC. 92256202, U22A20399, 22221001, 22075117, 22073038, 22005128), the 111 project 2.0 (BP1221004), the Science and Technology Major Program of Gansu Province (22ZD6GD060, 22ZD6FA006) and the Fundamental Research Funds for the Central Universities (lzujbky-2022-kb01, lzujbky-2021-sp59). The authors are thankful for the Supercomputing Center of Lanzhou University for providing the computing time and beam line BL14B1 (Shanghai Synchrotron Radiation Facility) for providing the beam time.

References

1 L. Yao, Z. Zeng, C. Cai, P. Xu, H. Gu, L. Gao, J. Han, X. Zhang, X. Wang, X. Wang, A. Pan, J. Wang, W. Liang, S. Liu, C. Chen and J. Tang, Strong Second- and Third-Harmonic Generation in 1D Chiral Hybrid Bismuth Halides, *J. Am. Chem. Soc.*, 2021, **143**, 16095.
2 S. Qi, P. Cheng, X. Han, F. Ge, R. Shi, L. Xu, G. Li and J. Xu, Organic-Inorganic Hybrid Antimony(III) Halides for Second Harmonic Generation, *Cryst. Growth Des.*, 2022, **22**, 6545.
3 A. Autere, H. Jussila, Y. Dai, Y. Wang, H. Lipsanen and Z. Sun, Nonlinear Optics with 2D Layered Materials, *Adv. Mater.*, 2018, **30**, 1705963.
4 M. Pawlicki, H. A. Collins, R. G. Denning and H. L. Anderson, Two-Photon Absorption and the Design of Two-Photon Dyes, *Angew. Chem., Int. Ed.*, 2009, **48**, 3244.
5 R. L. Gieseking, S. Mukhopadhyay, C. Risko, S. R. Marder and J. L. Brédas, 25th Anniversary Article: Design of Polymethine Dyes for All-Optical Switching Applications: Guidance from Theoretical and Computational Studies, *Adv. Mater.*, 2013, **26**, 68.
6 Y. Zhou, Y. Huang, X. Xu, Z. Fan, J. B. Khurgin and Q. Xiong, Nonlinear optical properties of halide perovskites and their applications, *Appl. Phys. Rev.*, 2020, **7**, 041313.
7 L. Mennel, M. M. Furchi, S. Wachter, M. Paur, D. K. Polyushkin and T. Mueller, Optical imaging of strain in two-dimensional crystals, *Nat. Commun.*, 2018, **9**, 516.

8 M. Thomaschewski and S. I. Bozhevolnyi, Pockels modulation in integrated nanophotonics, *Appl. Phys. Rev.*, 2022, **9**, 021311.
9 L. Caspani, C. Xiong, B. J. Eggleton, D. Bajoni, M. Liscidini, M. Galli, R. Morandotti and D. J. Moss, Integrated sources of photon quantum states based on nonlinear optics, *Light: Sci. Appl.*, 2017, **6**, e17100.
10 Y. Liu, Y. P. Gong, S. N. Geng, M. L. Feng, D. Manidaki, Z. Y. Deng, C. C. Stoumpos, P. Canepa, Z. W. Xiao, W. X. Zhang and L. L. Mao, Hybrid Germanium Bromide Perovskites with Tunable Second Harmonic Generation, *Angew. Chem., Int. Ed.*, 2022, **61**, e202208875.
11 N. Dehnhardt, M. Axt, J. Zimmermann, M. Yang, G. Mette and J. Heine, Band Gap-Tunable, Chiral Hybrid Metal Halides Displaying Second-Harmonic Generation, *Chem. Mater.*, 2020, **32**, 4801.
12 J. Ahn, E. Lee, J. Tan, W. Yang, B. Kim and J. Moon, A new class of chiral semiconductors: chiral-organic-molecule-incorporating organic-inorganic hybrid perovskites, *Mater. Horiz.*, 2017, **4**, 851.
13 D. Di Nuzzo, L. Cui, J. L. Greenfield, B. Zhao, R. H. Friend and S. C. J. Meskers, Circularly Polarized Photoluminescence from Chiral Perovskite Thin Films at Room Temperature, *ACS Nano*, 2020, **14**, 7610.
14 A. Pietropaolo, A. Mattoni, G. Pica, M. Fortino, G. Schifino and G. Grancini, Rationalizing the design and implementation of chiral hybrid perovskites, *Chem*, 2022, **8**, 1231.
15 F. Ge, B. H. Li, P. Cheng, G. Li, Z. Ren, J. Xu and X. H. Bu, Chiral Hybrid Copper(I) Halides for High Efficiency Second Harmonic Generation with a Broadband Transparency Window, *Angew. Chem., Int. Ed.*, 2022, **61**, e202115024.
16 J. Xu, X. Li, J. Xiong, C. Yuan, S. Semin, T. Rasing and X. H. Bu, Halide Perovskites for Nonlinear Optics, *Adv. Mater.*, 2020, **32**, 1806736.
17 D. Okada and F. Araoka, Manipulation of Chiral Nonlinear Optical Effect by Light-Matter Strong Coupling, *Nano Lett.*, 2024, **24**, 7443.
18 X. Cheng, S. Muthukrishnan, H. Mi, S. Deng, G. Serdaroğlu, R. Vidya and A. Stroppa, Mixed Organic Cation in Chiral Two-Dimensional Organic-Inorganic Hybrid Metal Halides-An Ab Initio Study of Nonlinear Optical (NLO) Properties, *J. Phys. Chem. C*, 2024, **128**, 11392.
19 G. K. Long, R. Sabatini, M. I. Saidaminov, G. Lakhwani, A. Rasmita, X. G. Liu, E. H. Sargent and W. B. Gao, Chiral-perovskite optoelectronics, *Nat. Rev. Mater.*, 2020, **5**, 423.
20 J. Bai, H. Wang, J. Ma, Y. Zhao, H. Lu, Y. Zhang, S. Gull, T. Qiao, W. Qin, Y. Chen, L. Jiang, G. Long and Y. Wu, Wafer-Scale Patterning Integration of Chiral 3D Perovskite Single Crystals toward High-Performance Full-Stokes Polarimeter, *J. Am. Chem. Soc.*, 2024, **146**, 18771.
21 S. Hu, B. Tang, S. V. Kershaw, N. A. Kotov and R. Andrey, Temperature Dependence of Charge Transport Properties of Quasi-2D Chiral Perovskite Thin-Film Field-Effect Transistors, *ACS Appl. Mater. Interfaces*, 2024, **16**, 12965.
22 S.-H. Yang, R. Naaman, Y. Paltiel and S. S. P. Parkin, Chiral spintronics, *Nat. Rev. Phys.*, 2021, **3**, 328.
23 S. H. Nam, J. An, W. Jeong, J. G. Oh, J. M. Luther, M. C. Beard, T. H. Han, I.-H. Park and Y.-H. Kim, Structural Asymmetry and Chiral-Induced Spin Selectivity in Chiral Palladium-Halide Semiconductors, *J. Am. Chem. Soc.*, 2024, **146**, 15045.
24 S. Mishra, E. G. Bowes, S. Majumder, J. A. Hollingsworth, H. Htoon and A. C. Jones, Inducing Circularly Polarized Single-Photon Emission via Chiral-Induced Spin Selectivity, *ACS Nano*, 2024, **18**, 8663.
25 J. Son, G. Jang, S. Ma, H. Lee, C. U. Lee, S. Yang, J. Lee, S. Moon, W. Jeong, J. H. Park, C. W. Jung, J. H. Kim, J. S. Park and J. Moon, Fluorinated Organic Cations Derived Chiral 2D Perovskite Enabling Enhanced Spin-Dependent Oxygen Evolution Reaction, *Adv. Sci.*, 2024, 2403326.
26 J. Cheng, G. Yi, Z. Zhang, Y. Long, H. Zeng, L. Huang, G. Zou and Z. Lin, In Situ Chiral Template Approach to Synthesize Homochiral Lead Iodides for Second-Harmonic Generation, *Angew. Chem., Int. Ed.*, 2024, **63**, e202318385.
27 J. Q. Zhou, P. R. Xie, C. Wang, T. Y. Bian, J. Chen, Y. Liu, Z. Guo, C. C. Chen, X. Pan, M. Luo, J. Yin and L. L. Mao, Hybrid Double Perovskite Derived Halides Based on Bi and Alkali Metals (K, Rb): Diverse Structures, Tunable Optical Properties and Second Harmonic Generation Responses, *Angew. Chem., Int. Ed.*, 2023, **62**, e202307646.
28 Y. Mao, S. Guo, X. Huang, K. Bu, Z. Li, P. Q. H. Nguyen, G. Liu, Q. Hu, D. Zhang, Y. Fu, W. Yang and X. Lü, Pressure-Modulated Anomalous Organic-Inorganic Interactions Enhance Structural Distortion and Second-Harmonic Generation in $MHyPbBr_3$ Perovskite, *J. Am. Chem. Soc.*, 2023, **145**, 23842.
29 X. W. Fu, Z. X. S. Zeng, S. L. Jiao, X. X. Wang, J. X. Wang, Y. Jiang, W. H. Zheng, D. L. Zhang, Z. H. Tian, Q. Y. Li and A. L. Pan, Highly Anisotropic Second-Order Nonlinear Optical Effects in the Chiral Lead-Free Perovskite Spiral Microplates, *Nano Lett.*, 2023, **23**, 606.
30 Z. Yu, S. Cao, Y. Zhao, Y. Guo, M. Dong, Y. Fu, J. Zhao, J. Yang, L. Jiang and Y. Wu, Chiral Lead-Free Double Perovskite Single-Crystalline Microwire Arrays for Anisotropic Second-Harmonic Generation, *ACS Appl. Mater. Interfaces*, 2022, **14**, 39451.
31 C. Yuan, X. Li, S. Semin, Y. Feng, T. Rasing and J. Xu, Chiral Lead Halide Perovskite Nanowires for Second-Order Nonlinear Optics, *Nano Lett.*, 2018, **18**, 5411.
32 D. Fu, J. Xin, Y. He, S. Wu, X. Zhang, X. M. Zhang and J. Luo, Chirality-Dependent Second-Order Nonlinear Optical Effect in 1D Organic-Inorganic Hybrid Perovskite Bulk Single Crystal, *Angew. Chem., Int. Ed.*, 2021, **60**, 20021.
33 Z. Guo, J. Li, J. Liang, C. Wang, X. Zhu and T. He, Regulating Optical Activity and Anisotropic Second-Harmonic Generation in Zero-Dimensional Hybrid Copper Halides, *Nano Lett.*, 2022, **22**, 846.
34 Z. H. Guo, J. Z. Li, R. L. Liu, Y. Yang, C. S. Wang, X. Zhu and T. C. He, Spatially Correlated Chirality in Chiral Two-Dimensional Perovskites Revealed by Second-Harmonic-Generation Circular Dichroism Microscopy, *Nano Lett.*, 2023, **23**, 7434.

35 H. B. Wang, J. Z. Li, H. L. Lu, S. Gull, T. Y. Shao, Y. X. Zhang, T. F. He, Y. S. Chen, T. C. He and G. K. Long, Chiral Hybrid Germanium(II) Halide with Strong Nonlinear Chiroptical Properties, *Angew. Chem., Int. Ed.*, 2023, **62**, e202309600.
36 J. J. Guan, Y. S. Zheng, P. X. Cheng, W. Q. Han, X. Han, P. H. Wang, M. Y. Xin, R. C. Shi, J. L. Xu and X. H. Bu, Free Halogen Substitution of Chiral Hybrid Metal Halides for Activating the Linear and Nonlinear Chiroptical Properties, *J. Am. Chem. Soc.*, 2023, **145**, 26833.
37 D. Okada and F. Araoka, Magneto-chiral Nonlinear Optical Effect with Large Anisotropic Response in Two-Dimensional Halide Perovskite, *Angew. Chem., Int. Ed.*, 2024, **63**, e202402081.
38 M.-Y. Wan, Y.-Z. Tang, Y.-H. Tan, F.-X. Wang, Y.-N. Li, L.-J. Wang, J. Liao and M.-N. Wang, Excellent Switchable Properties, Broad-Band Emission, Ferroelectricity, and High T_c in a Two-Dimensional Hybrid Perovskite: $(4,4\text{-DCA})_2PbBr_4$ Exploited by H/F Substitution, *Inorg. Chem.*, 2023, **62**, 12525.
39 X. L. Peng, R. R. Han, Y. Z. Tang, Y. H. Tan, X. W. Fan, F. X. Wang and H. Zhang, 1D Chiral Lead Bromide Perovskite with Superior Second-Order Optical Nonlinearity, Photoluminescence, and High-Temperature Reversible Phase Transition, *Chem. - Asian J.*, 2023, **18**, e202201206.
40 J. Q. Luo, Q. Q. Jia, G. Teri, M. M. Lun, Z. J. Wang, Z. X. Zhang, Y. Zhang and D. W. Fu, Chirality Extends Multiple-Channel Bistable Responses in Hybrid Perovskites, *ACS Mater. Lett.*, 2024, **6**, 452.
41 S. Smółka, M. Mączka, D. Drozdowski, D. Stefańska, A. Gągor, A. Sieradzki, J. K. Zaręba and M. Ptak, Effect of Dimensionality on Photoluminescence and Dielectric Properties of Imidazolium Lead Bromides, *Inorg. Chem.*, 2022, **61**, 15225.
42 C. Shen, D. Sun, Y. Dang, K. Wu, T. Xu, R. Hou, H. Chen, J. Wang and D. Wang, $(C_4H_{10}NO)PbX_3$ (X = Cl, Br): Design of Two Lead Halide Perovskite Crystals with Moderate Nonlinear Optical Properties, *Inorg. Chem.*, 2022, **61**, 16936.
43 Y. Zheng, J. Xu and X. H. Bu, 1D Chiral Lead Halide Perovskites with Superior Second-Order Optical Nonlinearity, *Adv. Opt. Mater.*, 2022, **10**, 2101545.
44 M. Mączka, J. K. Zaręba, A. Gągor, D. Stefańska, M. Ptak, K. Roleder, D. Kajewski, A. Soszyński, K. Fedoruk and A. Sieradzki, $[Methylhydrazinium]_2PbBr_4$, a Ferroelectric Hybrid Organic-Inorganic Perovskite with Multiple Nonlinear Optical Outputs, *Chem. Mater.*, 2021, **33**, 2331.
45 Y. Ma, J. Wang, W. Guo, S. Han, J. Xu, Y. Liu, L. Lu, Z. Xie, J. Luo and Z. Sun, The First Improper Ferroelectric of 2D Multilayered Hybrid Perovskite Enabling Strong Tunable Polarization-Directed Second Harmonic Generation Effect, *Adv. Funct. Mater.*, 2021, **31**, 2103012.
46 S. Liu, A. R. DeFilippo, M. Balasubramanian, Z. Liu, S. G. Wang, Y. S. Chen, S. Chariton, V. Prakapenka, X. Luo, L. Zhao, J. S. Martin, Y. Lin, Y. Yan, S. K. Ghose and T. A. Tyson, High-Resolution In-Situ Synchrotron X-Ray Studies of Inorganic Perovskite $CsPbBr_3$: New Symmetry Assignments and Structural Phase Transitions, *Adv. Sci.*, 2021, **8**, 2003046.
47 M. a Mączka, M. Ptak, A. Gągor, D. Stefańska, J. K. Zaręba and A. Sieradzki, Methylhydrazinium Lead Bromide: Noncentrosymmetric Three-Dimensional Perovskite with Exceptionally Large Framework Distortion and Green Photoluminescence, *Chem. Mater.*, 2020, **32**, 1667.
48 S. Govinda, B. P. Kore, M. Bokdam, P. Mahale, A. Kumar, S. Pal, B. Bhattacharyya, J. Lahnsteiner, G. Kresse, C. Franchini, A. Pandey and D. D. Sarma, Behavior of Methylammonium Dipoles in $MAPbX_3$ (X = Br and I), *J. Phys. Chem. Lett.*, 2017, **8**, 4113.
49 G. Wang, S. Mei, J. Liao, W. Wang, Y. Tang, Q. Zhang, Z. Tang, B. Wu and G. Xing, Advances of Nonlinear Photonics in Low-Dimensional Halide Perovskites, *Small*, 2021, **17**, 2100809.
50 X. Jia, Y. Zheng, P. Cheng, X. Han, L. Xu and J. Xu, Methylpiperazine based 0D chiral hybrid lead halides for second harmonic generation, *Dalton Trans.*, 2022, **51**, 7248.
51 M. Xin, P. Cheng, X. Han, R. Shi, Y. Zheng, J. Guan, H. Chen, C. Wang, Y. Liu, J. Xu and X. H. Bu, Resonant Second Harmonic Generation in Proline Hybrid Lead Halide Perovskites, *Adv. Opt. Mater.*, 2023, **11**, 2202700.
52 L. Mao, P. Guo, M. Kepenekian, I. Hadar, C. Katan, J. Even, R. D. Schaller, C. C. Stoumpos and M. G. Kanatzidis, Structural Diversity in White-Light-Emitting Hybrid Lead Bromide Perovskites, *J. Am. Chem. Soc.*, 2018, **140**, 13078.
53 Y. Ai, X. G. Chen, P. P. Shi, Y. Y. Tang, P. F. Li, W. Q. Liao and R. G. Xiong, Fluorine Substitution Induced High T_c of Enantiomeric Perovskite Ferroelectrics: (*R*)- and (*S*)-3-(Fluoropyrrolidinium)$MnCl_3$, *J. Am. Chem. Soc.*, 2019, **141**, 4474.
54 X. Li, J. M. Hoffman and M. G. Kanatzidis, The 2D Halide Perovskite Rulebook: How the Spacer Influences Everything from the Structure to Optoelectronic Device Efficiency, *Chem. Rev.*, 2021, **121**, 2230.
55 Z. Yuan, C. Zhou, Y. Tian, Y. Shu, J. Messier, J. C. Wang, L. J. van de Burgt, K. Kountouriotis, Y. Xin, E. Holt, K. Schanze, R. Clark, T. Siegrist and B. Ma, One-dimensional organic lead halide perovskites with efficient bluish white-light emission, *Nat. Commun.*, 2017, **8**, 14051.
56 X. Ji, S. Geng, S. Zhang, Y. Gong, X. Zhang, R. Li, Y. Liu, J. Chen, R. Chen, Z. Xiao and L. Mao, Chiral 2D Cu(I) Halide Frameworks, *Chem. Mater.*, 2022, **34**, 8262.
57 L. Zhou, J. F. Liao, Z. G. Huang, J. H. Wei, X. D. Wang, H. Y. Chen and D. B. Kuang, Intrinsic Self-Trapped Emission in 0D Lead-Free $(C_4H_{14}N_2)_2In_2Br_{10}$ Single Crystal, *Angew. Chem., Int. Ed.*, 2019, **58**, 15435.
58 K. Robinson, G. V. Gibbs and P. H. Ribbe, Quadratic Elongation: A Quantitative Measure of Distortion in Coordination Polyhedra, *Science*, 1971, **172**, 567.
59 S. Jiang, P. S. Zhao, G. X. Xing, H. M. Kang, X. L. Li, T. Z. Zhao, B. Li and T. Y. Zhang, Bismuth-Based Chiral Perovskite with Different Dimensions for Second-Order Nonlinear Optical Properties, *Adv. Opt. Mater.*, 2023, **11**, 2203078.
60 K. H. Jin, Y. Zhang, K. J. Li, M. E. Sun, X. Y. Dong, Q. L. Wang and S. Q. Zang, Enantiomorphic Single Crystals of Linear Lead(II) Bromide Perovskitoids with White Circularly Polarized Emission, *Angew. Chem., Int. Ed.*, 2022, **61**, e202205317.

61 Y. Wang, S. Guo, H. Luo, C. Zhou, H. Lin, X. Ma, Q. Hu, M. H. Du, B. Ma, W. Yang and X. Lu, Reaching 90% Photoluminescence Quantum Yield in One-Dimensional Metal Halide $C_4N_2H_{14}PbBr_4$ by Pressure-Suppressed Nonradiative Loss, *J. Am. Chem. Soc.*, 2020, **142**, 16001.
62 A. Biswas, R. Bakthavatsalam, S. R. Shaikh, A. Shinde, A. Lohar, S. Jena, R. G. Gonnade and J. Kundu, Efficient Broad-Band Emission from Contorted Purely Corner-Shared One Dimensional (1D) Organic Lead Halide Perovskite, *Chem. Mater.*, 2019, **31**, 2253.
63 B. Sun, Z. Yan, Y. Cao, S. S. Ding, R. J. Li, B. Ma, X. Y. Li, H. Yang, W. Yin, Y. M. Zhang, Q. Wang, X. F. Shao, D. Z. Yang, D. S. Xue and H. L. Zhang, Intrinsic Ferromagnetic Semiconductors with High Saturation Magnetization from Hybrid Perovskites, *Adv. Mater.*, 2023, **35**, 2303945.
64 W. T. Wu, X. Y. Shang, Z. J. Xu, H. Ye, Y. P. Yao, X. Y. Chen, M. C. Hong, J. H. Luo and L. N. Li, Toward Efficient Two-Photon Circularly Polarized Light Detection through Cooperative Strategies in Chiral Quasi-2D Perovskites, *Adv. Sci.*, 2023, **10**, 2206070.
65 J. Ahn, S. Ma, J.-Y. Kim, J. Kyhm, W. Yang, J. A. Lim, N. A. Kotov and J. Moon, Chiral 2D Organic Inorganic Hybrid Perovskite with Circular Dichroism Tunable Over Wide Wavelength Range, *J. Am. Chem. Soc.*, 2020, **142**, 4206.
66 Q. Wang, H. Zhu, W. Chen, J. Hao, Z. Wang, J. Tang, Y. Yang, X. W. Sun, D. Wu and K. Wang, Strong circularly polarized luminescence from quantum dots/2D chiral perovskites composites, *Nano Res.*, 2023, **16**, 7593.
67 H. M. Zhu, Q. Q. Wang, K. Sun, W. Chen, J. Tang, J. J. Hao, Z. J. Wang, J. Y. Sun, W. C. H. Choy, P. Muller-Buschbaum, X. W. Sun, D. Wu and K. Wang, Solvent Modulation of Chiral Perovskite Films Enables High Circularly Polarized Luminescence Performance from Chiral Perovskite/Quantum Dot Composites, *ACS Appl. Mater. Interfaces*, 2023, **15**, 9978.
68 R. Lu, Z. Wen, M. Zhao, J. Li, L. Zhang, Y. Yang, H. Jin, Y. Chen, S. Wang and S. Pan, Spacer Cation Alloying Enables Markedly Improved Chiroptical Properties of Two-Dimensional Chiral Hybrid Perovskite Nanosheets, *Adv. Opt. Mater.*, 2022, **11**, 2202290.
69 H. Lu, C. Xiao, R. Song, T. Li, A. E. Maughan, A. Levin, R. Brunecky, J. J. Berry, D. B. Mitzi, V. Blum and M. C. Beard, Highly Distorted Chiral Two-Dimensional Tin Iodide Perovskites for Spin Polarized Charge Transport, *J. Am. Chem. Soc.*, 2020, **142**, 13030.
70 L. Yan, M. K. Jana, P. C. Sercel, D. B. Mitzi and W. You, Alkyl-Aryl Cation Mixing in Chiral 2D Perovskites, *J. Am. Chem. Soc.*, 2021, **143**, 18114.
71 X. Han, P. Cheng, W. Han, R. Shi, J. Guan, G. Li and J. Xu, Circularly polarized luminescence and nonlinear optical harmonic generation based on chiral zinc halides, *Chem. Commun.*, 2023, **59**, 7447.
72 J. R. Heflin, C. Figura, D. Marciu, Y. Liu and R. O. Claus, Thickness dependence of second-harmonic generation in thin films fabricated from ionically self-assembled monolayers, *Appl. Phys. Lett.*, 1999, **74**, 495.
73 M. Zhu, M. Zhong, X. Guo, Y. Wang, Z. Chen, H. Huang, J. He, C. Su and K. P. Loh, Efficient and Anisotropic Second Harmonic Generation in Few-Layer SnS Film, *Adv. Opt. Mater.*, 2021, **9**, 2101200.
74 X. Fu, Z. Zeng, S. Jiao, X. Wang, J. Wang, Y. Jiang, W. Zheng, D. Zhang, Z. Tian, Q. Li and A. Pan, Highly Anisotropic Second-Order Nonlinear Optical Effects in the Chiral Lead-Free Perovskite Spiral Microplates, *Nano Lett.*, 2023, **23**, 606.
75 M. Bertolotti, A. Belardini, A. Benedetti and C. Sibilia, Second harmonic circular dichroism by self-assembled metasurfaces, *J. Opt. Soc. Am. B*, 2015, **32**, 1287.
76 X. Sun, J. Yang, L. Sun, G. Yang, C. Liu, Y. Tao, Q. Cheng, C. Wang, H. Xu and Q. Zhang, Tunable Reversal of Circular Dichroism in the Seed-Mediated Growth of Bichiral Plasmonic Nanoparticles, *ACS Nano*, 2022, **16**, 19174.
77 L. E. MacKenzie and P. Stachelek, The twists and turns of chiral chemistry, *Nat. Chem.*, 2021, **13**, 521.
78 S. J. Liu, L. Zhu, Y. H. Zhang, W. Chen, D. Zhu, P. Chen and Y. Q. Lu, Bi-Chiral Nanostructures Featuring Dynamic Optical Rotatory Dispersion for Polychromatic Light Multiplexing, *Adv. Mater.*, 2023, **35**, 2301714.
79 C. He, J. Qiu, Z. Mu, J. Chen, Y. Wu, Z. Jiang, P. Zhang, X. Qin, G. Xing and X. Liu, Room temperature circularly polarized emission in perovskite nanocrystals through bichiral-molecule-induced lattice reconstruction, *Matter*, 2024, **7**, 475.
80 C.-H. Yang, S.-B. Xiao, H. Xiao, L.-J. Xu and Z.-N. Chen, Efficient Red-Emissive Circularly Polarized Electroluminescence Enabled by Quasi-2D Perovskite with Chiral Spacer Cation, *ACS Nano*, 2023, **17**, 7830.
81 M. Zacharias and F. Giustino, One-shot calculation of temperature-dependent optical spectra and phonon-induced band-gap renormalization, *Phys. Rev. B*, 2016, **94**, 075125.
82 M. Zacharias, G. Volonakis, F. Giustino and J. Even, Anharmonic electron-phonon coupling in ultrasoft and locally disordered perovskites, *npj Comput. Mater.*, 2023, **9**, 153.
83 A. Maiti and A. J. Pal, Spin-Selective Charge Transport in Lead-Free Chiral Perovskites: The Key towards High-Anisotropy in Circularly-Polarized Light Detection, *Angew. Chem., Int. Ed.*, 2022, **61**, e202214161.
84 L. Yao, K.-H. Xue, H. Tong, C. Chen, G. Niu, W. Yang and J. Tang, Dimensional Control of Chiral Antimony Halide Compounds for Enhanced Circular Dichroism, *Cryst. Growth Des.*, 2022, **22**, 5552.
85 Y. Lou, S. Zhang, Z. Gu, N. Wang, S. Wang, Y. Zhang and Y. Song, Perovskite single crystals: Dimensional control, optoelectronic properties, and applications, *Mater. Today*, 2023, **62**, 225.
86 A. Ishii and T. Miyasaka, Direct detection of circular polarized light in helical 1D perovskite-based photodiode, *Sci. Adv.*, 2020, **6**, eabd3274.
87 D. Duan, C. Ge, M. Z. Rahaman, C.-H. Lin, Y. Shi, H. Lin, H. Hu and T. Wu, Recent progress with one-dimensional metal halide perovskites: from rational synthesis to optoelectronic applications, *NPG Asia Mater.*, 2023, **15**, 8.

88 P. Klement, N. Dehnhardt, C. D. Dong, F. Dobener, S. Bayliff, J. Winkler, D. M. Hofmann, P. J. Klar, S. Schumacher, S. Chatterjee and J. Heine, Atomically Thin Sheets of Lead-Free 1D Hybrid Perovskites Feature Tunable White-Light Emission from Self-Trapped Excitons, *Adv. Mater.*, 2021, **33**, 2100518.
89 S. Sun, M. Lu, X. Gao, Z. Shi, X. Bai, W. W. Yu and Y. Zhang, 0D Perovskites: Unique Properties, Synthesis, and Their Applications, *Adv. Sci.*, 2021, **8**, 2102689.
90 J. Yin, P. Maity, M. De Bastiani, I. Dursun, O. M. Bakr, J.-L. Brédas and O. F. Mohammed, Molecular behavior of zero-dimensional perovskites, *Sci. Adv.*, 2017, **3**, e1701793.